



# Robust triboelectric-electromagnetic hybrid nanogenerator with maglev-enabled automatic mode transition for exploiting breeze energy

Kangqi Fan<sup>a,b,\*</sup>, Chenggen Chen<sup>a,b</sup>, Baosen Zhang<sup>b</sup>, Xiang Li<sup>b</sup>, Zhen Wang<sup>a</sup>, Tinghai Cheng<sup>b,\*</sup>, Zhong Lin Wang<sup>b,c,\*</sup>

<sup>a</sup> School of Mechano-Electronic Engineering, Xidian University, Xi'an 710071, China

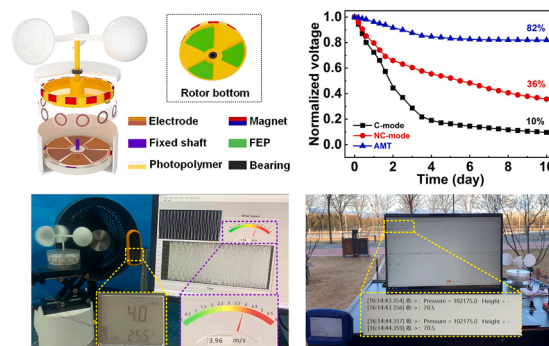
<sup>b</sup> Beijing Institute of Nanoenergy and Nanosystems, Chinese Academy of Sciences, Beijing 101400, China

<sup>c</sup> School of Materials Science and Engineering, Georgia Institute of Technology, Atlanta, GA 30332-0245, United States

## HIGHLIGHTS

- An automatic-mode-transition (AMT) strategy is proposed for breeze exploitation.
- The maglev-enabled AMT strategy achieves significantly reduced material abrasion.
- An AMT triboelectric-electromagnetic hybrid nanogenerator (AMT-TEHG) is developed.
- The AMT-TEHG can work under a low wind speed of 2.4 m/s.
- The AMT-TEHG achieves very high mechanical durability and electrical stability.

## GRAPHICAL ABSTRACT



## ARTICLE INFO

### Keywords:

Triboelectric nanogenerator  
Low-power electronics  
Maglev mechanism  
Hybrid generator  
Breeze energy

## ABSTRACT

Exploiting the pervasive breeze energy is normally difficult due to the high start-up wind speed of the conventional electromagnetic generator (EMG) and the material abrasion of the emerging triboelectric nanogenerator (TEHG). We report herein an automatic-mode-transition (AMT) strategy, which enables the TEHG to work in intermittent-contact (IC) mode under a low wind speed of 2.4 m/s and automatically transition to noncontact (NC) mode with the increasing wind speed. Realized with a rationally designed maglev mechanism, the AMT-TEHG can replenish the dissipated charges with very small friction drag and minute material abrasion, contributing to a low start-up speed, high mechanical durability, and enhanced electrical stability. During a 10-day durability test, the AMT-TEHG can maintain 82 % of its incipient voltage; by contrast, the NC-TEHG and C-TEHG only retain 36 % and 10 % output voltage, respectively. The AMT-TEHG can be upgraded easily to an AMT triboelectric-electromagnetic hybrid nanogenerator (AMT-TEHG) by simply adding pick-up coils, allowing the device to generate complementary electric outputs. By exploiting the breeze energy, the AMT-TEHG can serve not only as a self-sufficient wind speed sensor but also as a green energy source for some electronics. This work demonstrates a promising strategy for realizing robust TEHGs, which has great potential in breeze energy exploitation and self-sufficient sensing.

\* Corresponding authors.

E-mail addresses: [kangqifan@gmail.com](mailto:kangqifan@gmail.com) (K. Fan), [chengtinghai@binn.cas.cn](mailto:chengtinghai@binn.cas.cn) (T. Cheng), [zhong.wang@mse.gatech.edu](mailto:zhong.wang@mse.gatech.edu) (Z. Lin Wang).

<https://doi.org/10.1016/j.apenergy.2022.120218>

Received 15 March 2022; Received in revised form 26 September 2022; Accepted 23 October 2022

Available online 4 November 2022

0306-2619/© 2022 Elsevier Ltd. All rights reserved.

## 1. Introduction

With the continuous reduction of fossil fuels and ever increasing concern on environmental contamination, the renewable wind energy has gained the attention of worldwide researchers owing to its extensive availability and pollution-free virtue. The wind energy has been harvested and converted into electricity by bulky wind generators that work as concentrated power plants and deliver electric energy to users via cables or power grids [1]. On the other hand, human society has stepped into the era of Internet of Things (IoTs) [2,3], which is characterized by trillions of decentralized sensors with dispersed power supply requirements to monitor both human livings and ambient environment [4,5]. Up to now, these numerous sensors have been powered mainly by energy-limited batteries, leading to high operation cost and potential environmental harm [6]. A straightforward strategy to overcome this dilemma is reducing the size of the conventional wind generator to achieve distributed power source for these sensors. However, downscaling the conventional wind generator is difficult due to the complicated gear train employed for up-converting the rotation speed of the generator. Moreover, the noise and comparatively high start-up wind speed ( $>3.0$  m/s) make the undersized wind turbine a poor tool to scavenge the pervasive wind energy as a renewable green energy source for the huge number of sensors since the average wind speed close to the ground is just about 3.0 m/s [7]. Therefore, a clear technical gap appears between the power requirements of IoTs and the conventional power supplies [8].

Invented by Wang's group in 2012 [9], the triboelectric nanogenerator (TEHG), which works on the basis of Maxwell's displacement current [10,11], provides an excellent solution to the crucial drawbacks of the downscaled wind turbines due to TEHG's high voltage output under low-frequency/speed excitations, simple structure, light weight, and low cost [12–14]. Owing to the universal triboelectrification phenomenon even between liquids and solids [15–17], there is little restriction for the selection of materials to construct diverse TEHGs for applications in a series of fields, such as self-sufficient sensors [5,18,19], human-machine interaction [20,21], smart agriculture [5,22], wind energy [23,24], and blue energy [25,26]. For the exploitation of wind energy, the rotary sliding TEHGs (RS-TEHGs) have been widely employed due to the high energy harvesting performance [27–29], but the sliding friction between the triboelectric layers normally brings about undesired energy dissipation, material abrasion, comparatively large wind speeds for driving the RS-TEHGs, low output stability, and shortened working duration. Therefore, reducing the sliding friction and minimizing the material abrasion are pivotal for developing such RS-TEHGs that can exploit wind energy with extended service lifetime and high output stability.

By separating the dielectric film and the electrode layer, the non-contact TEHG design can avert the material abrasion and friction loss, but the gradually decayed charges pre-injected in the dielectric film lead to degenerative electric outputs [30,31]. To achieve stable electric outputs and in the meanwhile low frictional resistance, the rolling friction [32–34] and soft contact [35–37] between the dielectric film and the electrode layer have been adopted in the design of rotary TEHGs. By reducing the friction coefficient or contact force between the tribo-materials, the friction drag and material wear can be alleviated to some extent. In recent years, the intermittent-contact RS-TEHG strategy [38–40], which switches automatically between contact mode and noncontact mode, seems to provide a more ideal solution to the aforementioned challenges of the RS-TEHGs. The intermittent-contact RS-TEHG can work in the contact mode to regenerate and replenish the dissipated charges at low rotation speeds and switch to the noncontact mode when the rotation speed is high. As a result, high output stability can be achieved only at the cost of slight material abrasion. However, to exploit the discontinuous natural wind energy, the RS-TEHG is required to be frequently activated from the idle state or contact mode by comparatively high wind speeds, which gives rise to low utilization

efficiency of wind energy because the average wind speed near the ground is approximately 3.0 m/s [7]. To fill the knowledge gap between the high electric outputs and long working duration of the RS-TEHG, an ingenious RS-TEHG that can not only switch its working mode automatically but also achieve significant reduction in the friction resistance is highly demanded.

In this work, an automatic-mode-transition (AMT) rotary triboelectric-electromagnetic hybrid nanogenerator (AMT-TEHG) with significantly improved electrical stability and mechanical durability is proposed to achieve efficient harvesting of breeze energy. Enabled by a rationally designed maglev mechanism, the AMT-TEHG can work in intermittent-contact mode (IC-mode) under a low wind speed of 2.4 m/s and automatically transition into noncontact mode (NC-mode) with the increasing wind speed. Owing to the intermittent contact between tribo-materials at low wind speeds, the dissipated charges can be replenished with low friction resistance and minute material abrasion, achieving enhanced electrical stability and mechanical durability for the TEHG. By adding pick-up coils to the maglev mechanism, the AMT-TEHG can be easily achieved, which enables the device to generate electricity simultaneously through two transduction mechanisms. As driven by 5.0 m/s wind, the TEHG unit achieves a high power density of 449.5 mW/kg. Under various low wind speeds, the AMT-TEHG has a high energy conversion efficiency of around 12.3 %, making it well suited for the harvesting of breeze energy. We have also demonstrated some practical applications of the AMT-TEHG, such as powering a hygromograph, lighting up 280 LEDs, driving a pressure-altitude sensor, and working as a self-sufficient wind speed sensor. This study provides a promising strategy to realize automatic working mode transition with intent to improve the mechanical durability and lower the start-up wind speed for the effective exploitation of breeze energy.

## 2. Results and discussion

### 2.1. AMT-TEHG structure and working principle

Converting the widely distributed wind energy into electric outputs can not only enable the measurement of wind speed but also supply electric power to other sensors for monitoring the ambient environment. For the rotary electromagnetic generator (EMG), the voltage signal is weak in the breeze scenario since the change rate of the magnetic flux across the pick-up coils is low due to the slow rotation of the rotor relative to the stator. Consequently, extracting the wind speed information from the voltage signal or utilizing it as a power source for other sensors is rather difficult. The RS-TEHG, on the other hand, can generate high voltage signal even under low-speed rotation, but the sliding friction between the tribo-materials brings about poor mechanical durability and comparatively high start-up wind speeds. The non-contact rotary TEHG can perform well as driven by breeze, but the gradual dissipation of pre-injected charges on the dielectric films leads to unstable electric outputs. In this context, we report an AMT-TEHG design enabled by a maglev mechanism to reduce the start-up wind speed and in the meanwhile improve the device robustness (mechanical durability and electrical stability).

The basic configuration of the AMT-TEHG consists of a rotor, a stator, and three wind cups, which are coaxially assembled with the rotor and stator being encapsulated in a cylindrical housing, as depicted in Fig. 1a. The rotor comprises a circular array of magnets, a hollow shaft, and three fan-shaped Fluorinated Ethylene Propylene (FEP) films uniformly bonded to the bottom of the rotor. The stator includes a fixed shaft, two radially-arrayed copper electrode networks attached to the top surface of a substrate, a circular array of magnets embedded in the substrate, and multiple sets of pick-up coils arranged in a ring. All the magnets embedded in both the rotor and the stator are magnetized along the radial direction. The three wind cups are connected to the rotor through a rotating shaft to capture the wind energy and spin the rotor. The rotating shaft is assembled with the lid of the housing via a ceramic

bearing. The hollow shaft of the rotor is mounted on the fixed shaft of the stator. To allow the rotor to move up and down along with the rotation, the rotating shaft of the wind cups has a diameter slightly smaller than the inner diameter of the bearing, and the hollow shaft of the rotor is designed with an inner diameter slightly larger than the (outer) diameter of the fixed shaft. Consisting of a TENG unit (FEP films and electrode layer) and an EMG unit (movable magnets and pick-up coils), the proposed AMT-TEHG can generate electricity simultaneously through two transduction mechanisms. The fabricated AMT-TEHG prototype is pictured in Fig. 1b, the main body (without the wind cups) of which is just 40 mm high and 82 mm in diameter, contributing to superior portability and easy integration with other electronics. The detailed information about the fabrication of the device is given in Section 4.

The automatic working mode transition of the AMT-TEHG is attributed to the repulsive interaction between the magnets in the rotor and

those in the stator. To show this, the magnetic interaction between a rotor with 12 cuboidal magnets (Nd-Fe-B,  $10 \times 6 \times 2 \text{ mm}^3$  for each) and a stator with 4 cuboidal magnets (Nd-Fe-B,  $10 \times 6 \times 2 \text{ mm}^3$  for each) is calculated via an analytical model [41], as illustrated in Fig. 1c. With all the magnets being magnetized along the radial direction, the rotor will reach the highest position when the magnets in the rotor align vertically with those in the stator due to the large repulsive force. On the contrary, under the influence of the gravity, the rotor slips to the lowest position if certain misalignment between the magnets in the rotor and those in the stator occurs. Since the magnets in both the rotor and the stator are arranged in a ring, the rotor will experience circularly undulant repulsive force (maglev force) from the stator as it rotates with respect to the stator. As a result, vertical oscillation of the rotor occurs along with its rotation owing to the interaction between the maglev force and the rotor gravity, as displayed in Fig. S1 and Movie S1. The motion of the rotor can be described by a dynamic model given in Note S1, which shows that

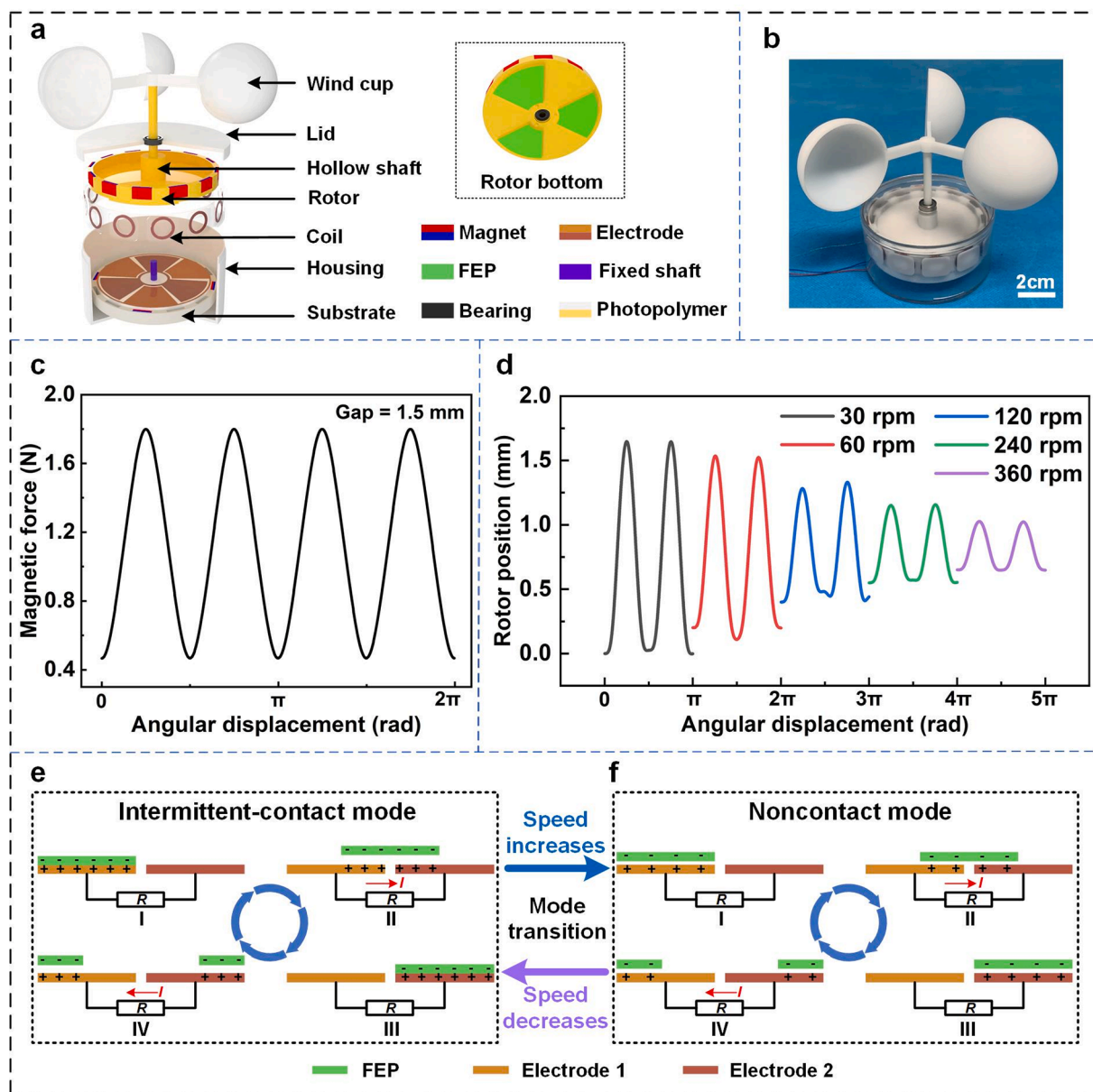


Fig. 1. AMT-TEHG structure and working principle. (a) Exploded view of the AMT-TEHG (The inset shows the arrangement of the FEP films). (b) A picture of the AMT-TEHG prototype. (c) The rotor–stator magnetic force with a vertical gap of 1.5 mm between the rotor magnets and stator magnets. (d) The vertical oscillation of the rotor at different rotation speeds (take the upper surface of the electrode layer as the reference height). Working principle of the TENG for (e) triboelectrification process in the IC-mode and (f) electrostatic induction in the NC-mode.

the vertical oscillation amplitude declines with an increase in the rotation speed, as plotted in Fig. 1d.

With the maglev mechanism, tribo-charges can be generated to replenish the lost charges pre-reserved on the dielectric films through the sliding contact between the dielectric films and the electrodes when the rotor moves toward its lowest position. The rotor will separate from the stator as the rotor rotates away from its lowest position under the action of the maglev force. In this way, the intermittent-contact working mode can be realized in the AMT-TEHG. It should be noted that the vertical oscillation of the rotor declines with the increasing rotation speed (Movie S1 and Fig. 1d), and the AMT-TEHG will go into the NC-mode if the rotation speed is high because there is no sufficient time for the rotor to move to the lowest position. Nevertheless, this is a beneficial outcome because the NC-mode can circumvent the friction drag and severe material abrasion induced by the high-speed sliding friction between tribo-materials.

For the TENG working in the contact mode (C-mode), the sliding friction of the FEP film relative to the copper electrodes generates positive charges on the electrodes and opposite charges of the same amount on the FEP films owing to the triboelectrification effect [42]. As the FEP slides between two electrodes, the generated positive charges will flow in a circuit connected to the two electrodes under the action of the electrostatic induction. Working in the sliding contact mode, the TENG can deliver the highest instantaneous electric power [43], but the friction heat and material wear lead to poor mechanical durability and reduced life span [14]. In the noncontact working mode, positive charges can also be driven to flow in the circuit when the FEP with negative charges sweeps over the two electrodes alternately. Although the friction resistance and material wear can be effectively averted in the NC-mode, the gradual dissipation of the charges on the FEP surface gives rise to degenerative electric outputs. For the proposed AMT-TEHG, owing to the maglev mechanism, the intermittent sliding contact between the FEP film and copper electrodes can be realized when the rotation speed is low, as illustrated in Fig. 1e. For this reason, the charges on the FEP surface can be replenished with very low friction resistance and significantly reduced material abrasion, which is also conducive to the reduction of the start-up wind speed. With an increase in the rotation speed, the device transforms gradually to the NC-mode and generates electric outputs without causing any material abrasion and friction resistance between the FEP films and electrodes, as shown in Fig. 1f. The potential differences between the two electrodes under IC and NC modes are also obtained by finite element method, as shown in Fig. S2, which is the cause of the current in the external circuit. Thus, with the maglev mechanism, improved mechanical durability and high electrical stability of the TENG can be achieved along with a low start-up wind speed.

## 2.2. Performance of the maglev mechanism

To exhibit the automatic working mode transition of the AMT-TEHG, a motor was first used to spin the AMT-TEHG with accurately controlled rotation speeds. This test was performed by removing the wind cups and rotating the rotor with a plectrum connected to the motor shaft. For the maglev mechanism with 12 magnets embedded in the rotor, a matched number (e.g., 3, 4, and 6) of magnets are required to be uniformly arranged in the stator to provide symmetrical forces to the rotor and hence avoid the inclination of the rotor relative to the stator, as illustrated in Fig. S3. For the case that three magnets are arranged in the stator, no distinct variation can be observed in the open-circuit voltage  $VT_{OC}$  and transferred charge  $QT_{SC}$  of the TENG unit when the rotor speed is increased from 30 rpm (round per minute) to 480 rpm, as shown in Fig. S4, indicating that the device works in the C-mode even at a high rotation speed of 480 rpm. When four magnets are arranged in the stator,  $VT_{OC}$  and  $QT_{SC}$  drop down quickly with increasing the rotation speed from 30 rpm to 60 rpm, and then almost keep constant with increasing the rotation speed >60 rpm, as exhibited in Fig. 2a,b,

respectively. The sudden reduction in  $VT_{OC}$  and  $QT_{SC}$  is induced by the switch from the intermittent-contact state to the noncontact state as the rotation speed is enhanced to 60 rpm. The AMT-TEHG then works in the NC-mode and generates nearly stable outputs of  $VT_{OC}$  and  $QT_{SC}$  under a higher rotation speed. If the number of the magnets arranged in the stator is increased to six, the large maglev force makes the AMT-TEHG work in the NC-mode regardless of the rotation speed, resulting in scarcely changed outputs of  $VT_{OC}$  and  $QT_{SC}$  for various rotation speeds, as shown in Fig. S5. For various numbers of magnets arranged in the stator, the short-circuit current of the TENG unit  $IT_{SC}$  grows continuously with an increase in the rotation speed of the rotor due to the increasing flow rate of the charges under the action of the electrostatic induction, as shown in Fig. 2c, Fig. S4 and Fig. S5.

To explore the feasibility of the automatic-mode-transition strategy in the breeze energy exploitation, we also measured the electric outputs of the TENG unit ( $VT_{OC}$ ,  $QT_{SC}$ , and  $IT_{SC}$ ) as driven by wind of various speeds. When three magnets are arranged in the stator, the AMT-TEHG cannot be activated by the wind with a speed lower than 3.0 m/s because the limited wind force cannot counteract the friction between the rotor and stator, as exhibited in Fig. S6. The AMT-TEHG starts to work in the C-mode and delivers comparatively high electric outputs in the case that the wind speed reaches 3.5 m/s, but the transition in the working mode cannot be achieved even if the wind speed is increased to 5.0 m/s. When the rotor in the AMT-TEHG is suspended by a stator with four magnets, the device can deliver comparatively high electric outputs under a low wind speed of 2.4 m/s due to the increased magnetic levitation force and hence reduced friction resistance, as shown in Fig. 2d-f. When the wind speed is increased to 3.0 m/s, a sudden drop in the values of  $VT_{OC}$  and  $QT_{SC}$  occurs as the AMT-TEHG switches from the IC-mode to the NC-mode. The working mode transition brings about significantly reduced friction resistance, which in conjunction with the increasing wind force boosts the sudden rise of the rotation speed and thus the value of  $IT_{SC}$ . With a further increase in the wind speed from 3.0 m/s, the AMT-TEHG works all the way in the NC-mode. The slight decline in  $VT_{OC}$  and  $QT_{SC}$  with the increasing wind speed is caused by the minute increase of the gap between the rotor and stator under the action of the magnetic levitation force. For the device with six magnets arranged in the stator, it can only work in the NC-mode due to the overly large levitation force, as shown in Fig. S7. In this case, the start-up wind speed of the device can be as low as 1.5 m/s, but the electrical stability cannot be guaranteed due to the gradual dissipation of charges pre-injected on the dielectric materials. To implement the automatic working mode transition for realizing robust TENGs and in the meanwhile achieve low start-up wind speeds for effectively exploiting the breeze energy, the device with four magnets arranged in the stator is adopted as our final design.

With four magnets embedded in the stator, the AMT-TEHG can be activated to work in the IC-mode from the idle state as triggered by wind of 2.4 m/s, and then transition into the NC-mode as the wind speed rises continuously from 2.4 to 5.0 m/s, as shown in Fig. 2g-i. A sudden drop in both  $VT_{OC}$  and  $QT_{SC}$  happens when the AMT-TEHG switches from the IC-mode to the NC-mode since the friction area fades away during this automatic transition process. Similar to the observation in Fig. 2f, the value of  $IT_{SC}$  in this test also ascends steadily as the device goes into the NC-mode from the IC-mode. Working in the NC-mode with large rotation speeds as triggered by wind of higher than 3.0 m/s, the TENG unit can provide stable and dense electric outputs without causing any sliding friction and material wear. Therefore, from the aforementioned analysis, three advantages of the maglev-based TENG unit can be identified: (1) a low start-up wind speed (2.4 m/s); (2) superior electrical stability enabled by the IC-mode under a low wind speed; (3) improved mechanical durability owing to the NC-mode in a broad range of wind speeds ( $\geq 3.0$  m/s).

It should be noted that the TENG outputs shown in Fig. 2 were all measured after the coils were introduced into the device. In order to figure out the effect of adding the coils on the rotor motion and TENG

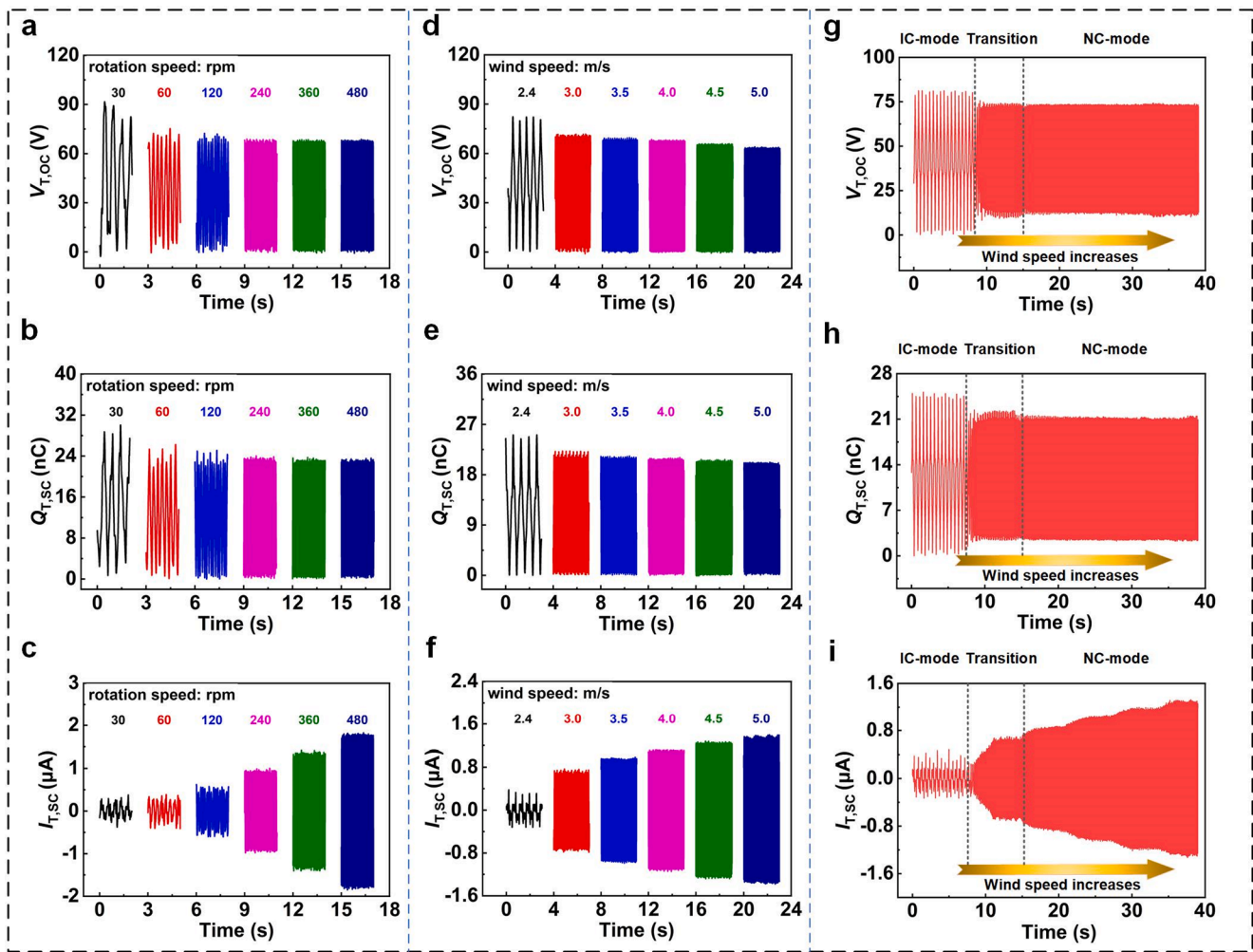


Fig. 2. Performance of the maglev mechanism with four magnets arranged in the stator. (a) Open-circuit voltage, (b) transferred charge and (c) short-circuit current of the TENG unit as excited by a motor. (d) Open-circuit voltage, (e) transferred charge and (f) short-circuit current of the TENG unit as driven by wind. (g) Open-circuit voltage, (h) transferred charge and (i) short-circuit current of the TENG unit as the wind speed goes up continuously from 2.4 to 5.0 m/s.

outputs, the voltage and current outputs of the TENG before adding the coils (uncoupled condition) and after adding the coils (coupled condition) were also measured at different wind speeds, as shown in Fig. S8. It can be observed that, for a given wind speed, there is no significant difference in the voltage and current outputs of the TENG unit under the two different conditions. Therefore, introducing the coils into the device has negligible effect on the rotor motion and TENG outputs.

### 2.3. Output characteristics of the TENG unit

Considering that the AMT-TEHG is proposed to exploit the breeze energy, special attention is paid to the output characteristics of the device under comparatively low wind speeds. For the TENG unit, the current declines continuously but the voltage  $V_{T,R}$  grows monotonously with an increase in the load resistance under a constant wind speed of 5.0 m/s, as displayed in Fig. 3a. The peak value of instantaneous power of the TENG unit  $P_T$  first grows with the electric load in the range from 0.2 to 200 M $\Omega$ , crests (0.23 mW) at 200 M $\Omega$ , and then goes down as the electric load  $R$  is increased beyond 200 M $\Omega$ . The instantaneous value of  $P_T$  is calculated by

$$P_T(t) = I_{T,R}^2(t)R \quad (1)$$

where  $I_{T,R}(t)$  is the current running through the electric load.

The TENG output power as a function of the electric load under various wind speeds is depicted in Fig. 3b, which indicates that the

TENG unit can deliver the optimal power if a load of around 200 M $\Omega$  is utilized. For a given electric load of 200 M $\Omega$ , the output charge  $Q_{T,R}$  descends from 21.6 to 17.4 nC with increasing the wind speed from 2.4 to 5.0 m/s, as exhibited in Fig. 3c. As the wind speed rises from 2.4 to 3.0 m/s, a comparatively large drop in the output charge is attributed to the transition of the AMT-TEHG from the IC-mode to the NC-mode. Increasing the wind speed beyond 3.0 m/s, the slight decay in the output charge is caused by the tiny increase in the gap between the rotor and stator under a higher wind speed. Within the same wind speed region from 2.4 to 5.0 m/s, the output power grows almost linearly from 0.04 to 0.23 mW due to the ever increasing wind energy.

Under various wind speeds, the open-circuit voltage and short-circuit charge of the TENG unit in different working modes are depicted in Fig. 3d,e, respectively, where the NC-mode is realized by arranging six magnets in the stator. It is worth mentioning that the perfect C-mode with no magnets positioned in the stator gives rise to an overly large contact force and friction resistance between the rotor and stator, which disables the device even under a comparatively high wind speed of 5.0 m/s. To address this issue, two magnets are arranged in the stator, which reduces the friction resistance and then enables the device to work in the C-mode as excited by wind of 4.5 m/s, as shown in Fig. S9. Therefore, the C-mode means that two magnets are positioned in the stator. It is apparent that the C-mode TENG can provide the highest output voltage under the effect of the contact electrification, but the high start-up wind speed makes the device incompetent for the effective harvesting of

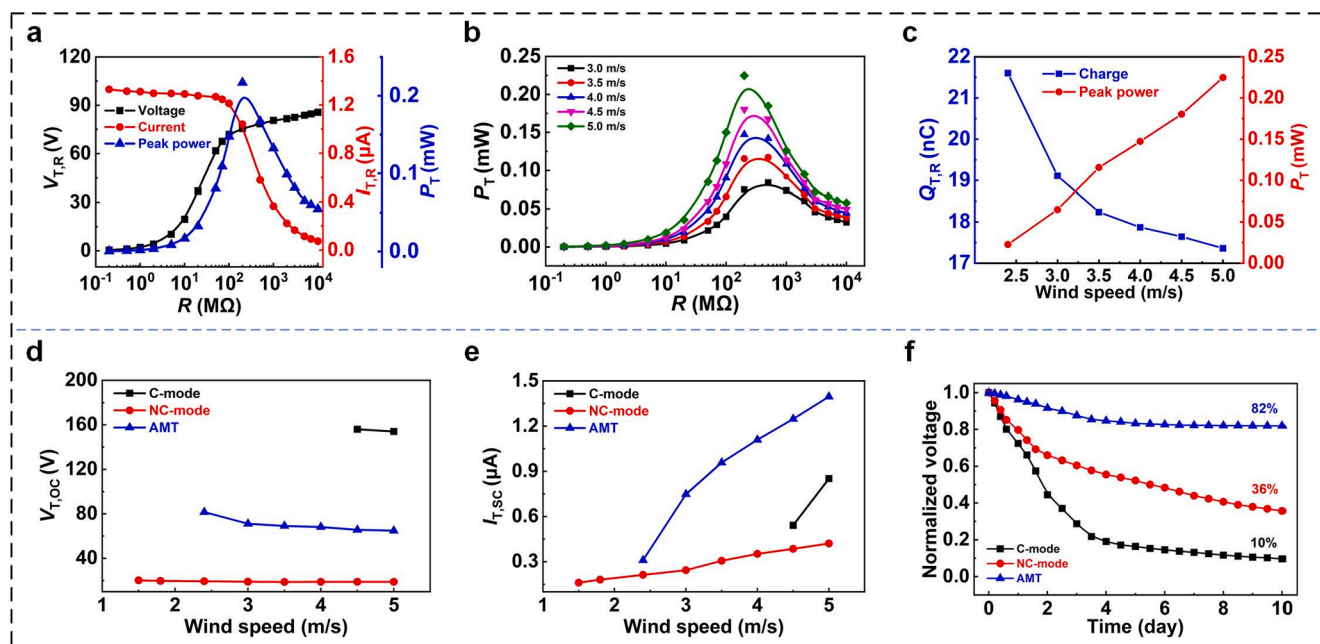


**Fig. 3.** Output characteristics of the TENG unit designed with the maglev mechanism. (a) Load voltage, load current, and output power as a function of electric load under a wind speed of 5.0 m/s. (b) Output power as a function of electric load under various wind speeds. (c) Output charge and output power as a function of wind speed. (d) Open-circuit voltage in various working modes. (e) Short-circuit current in various working modes. (f) Electrical stability in various working modes.

breeze energy. Normally, the short-circuit current of the rotary TENG grows with the rotation speed as the FEP films can contact/sweep the electrodes more frequently under a higher rotation speed [44]. For the C-mode TENG in this study, it fails to generate the highest output current due to the reduced rotation speed induced by the friction resistance. Although the NC-mode TENG can start to work as driven by 1.5 m/s wind, the very low electric outputs pose high difficulty for their efficient utilization. The TENG with automatic working mode transition, on the other hand, can achieve a comparatively low start-up wind speed of 2.4 m/s, intermediate output voltage, and high output current, making it a superior candidate for the effective exploitation of breeze energy.

Owing to the automatic transition from the IC-mode to the NC-mode as the wind speed rises from 2.4 to 3.0 m/s, the AMT-TENG can maintain around 82 % of its initial voltage after 10-day durability test, exhibiting superior electrical stability, as illustrated in Fig. 3f. In the test, the AMT-TENG, C-mode TENG and NC-mode TENG were exposed to the wind of 5.0 m/s from the idle state for two hours per day, and this test was performed continuously for ten days. By comparison, during the 10-day test, the normalized voltage of the C-mode TENG and the NC-mode TENG declines quickly to 10 % and 36 %, respectively. Pictures of the tribo-materials before and after the 10-day test are shown in Fig. S10. Compared with the C-mode TENG, the AMT-TEHG only leads to slight material abrasion, exhibiting excellent mechanical durability. The durability of TENGs with typical working modes has been given in Table S1, from which the improved durability of the AMT-TEHG in extended time is also evident.

#### 2.4. Output characteristics of the EMG unit

The EMG unit works on the basis of the electromagnetic induction effect, as illustrated in Fig. 4a. For a stationary coil, the magnetic flux through it increases as a magnet rotates toward it along with the rotor, which induces such an electric current in the coil that the consequent magnetic field impedes the increase of the magnetic flux through the coil (stage I). As the magnet rotates away from the stationary coil, the magnetic flux through the coil declines and hence the direction of the current in the coil reverses in a way to supplement the declined magnetic flux through the coil (stage II). With the continuous rotation of the rotor,

the next adjacent magnet first approaches and then deviates from the coil, inducing a current to flow in the coil with alternating directions once again (stage III and IV). In this way, alternating-current (AC) electric outputs will be generated with high frequencies under the continuous rotation of the rotor. Moreover, the electric output magnitude of the EMG unit grows with the increasing rotation speed of the rotor since it is positively dependent on the change rate of the magnetic flux crossing the coils [45].

With three magnets arranged in the stator, the large friction resistance between the rotor and the stator leads to not only a high start-up wind speed (3.5 m/s) but also low electric outputs, as shown in Fig. S11. By positioning six magnets in the stator, the device can start to work when driven by 1.5 m/s wind, as demonstrated in Fig. S12, but the low voltage converted from the low-speed wind by the EMG unit is difficult to be utilized in implementing self-sufficient sensor systems. By arranging four magnets in the stator, the start-up wind speed of the device can be as low as 2.4 m/s, and the open-circuit voltage  $V_{E,OC}$  and short-circuit current  $I_{E,SC}$  of the EMG unit go up from 0.31 V/0.68 mA to 3.95 V/8.74 mA with the rise of the wind speed from 2.4 to 5.0 m/s, as plotted in Fig. 4b,c, respectively. In this case, the output voltage of the EMG unit is still low under low-speed wind, but this downside can be easily overcome by the very high output voltage generated by the TENG unit. Moreover, for the device working in the NC-mode under comparatively high wind speeds (>3.0 m/s), no significant difference can be observed in the electric outputs of the EMG unit when the number of the stator magnets is increased from four to six. Therefore, by arranging four magnets in the stator, the maglev mechanism-enabled AMT strategy endows the device with a series of advantages, including significantly reduced friction resistance, enhanced mechanical durability, and complementary electric outputs from the TENG unit and EMG unit.

When the device is driven by the wind of 5.0 m/s, the EMG unit generates such a voltage that goes up monotonously with the rise of the load resistance from 1 to 8000  $\Omega$ , whereas the generated current has an opposite variation trend in the same resistance range, as plotted in Fig. 4d. Under the same excitation, the maximum output power of around 6.96 mW can be achieved by the EMG unit with an electric load of 500  $\Omega$ , deviating from which the output power falls off. The peak power of the EMG unit  $P_E$  as a function of the electric load  $R$  under

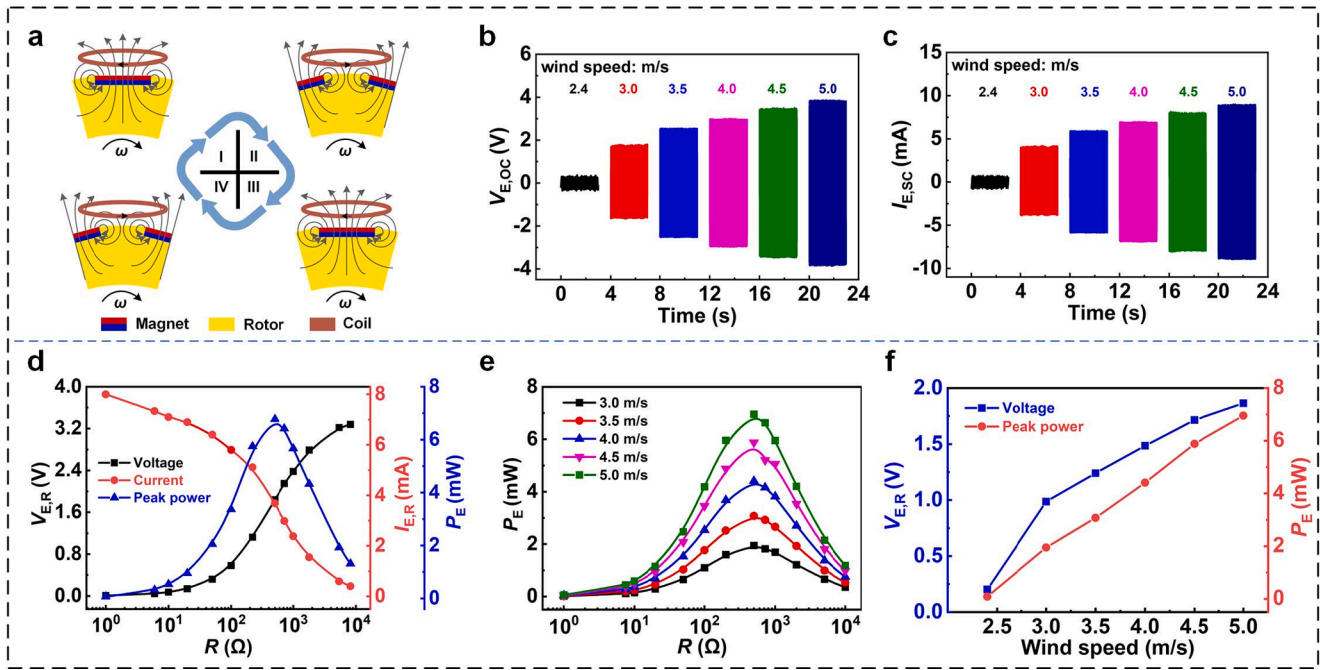


Fig. 4. Output characteristics of the EMG unit. (a) Magnetic induction lines and induced coil current at four typical stages. (b) Open-circuit voltage under various wind speeds. (c) Short-circuit current under different wind speeds. (d) Load voltage, load current, and output power as a function of electric load under 5.0 m/s wind. (e) Output power as a function electric load under various wind speeds. (f) Load voltage and output power as a function of wind speed.

various wind speeds is depicted in Fig. 4e, where the instantaneous value of  $P_E$  is obtained by.

$$P_E(t) = I_{E,R}^2(t)R \quad (2)$$

where  $I_{E,R}(t)$  is the current running through the electric load. It can be observed that, under various wind speeds, the output power is maximized at a load resistance of approximately 500  $\Omega$ . As the wind

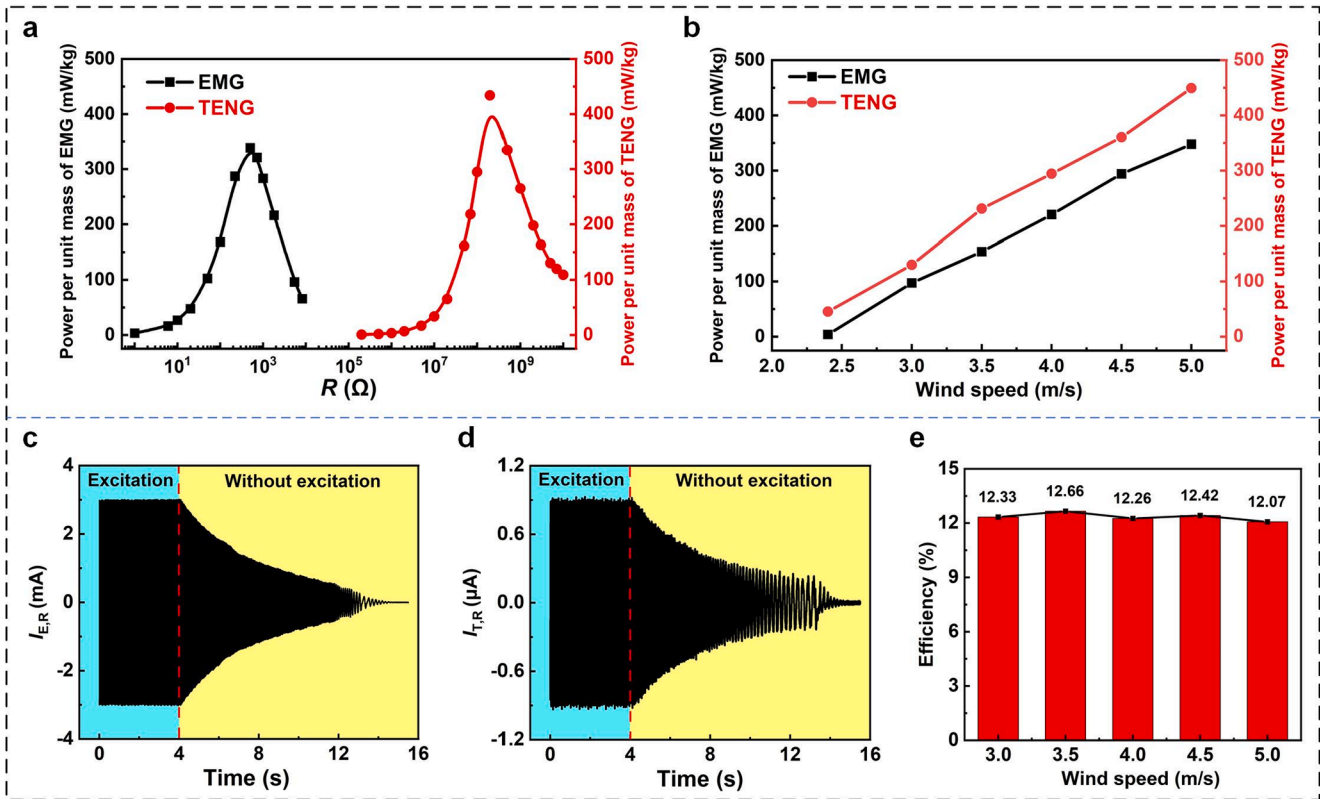


Fig. 5. Performance of the AMT-TEHG. (a) Weight power density of the EMG unit and TENG unit versus load resistance under 5.0 m/s wind. (b) Weight power density of the EMG unit and TENG unit versus wind speed. Output current of the EMG unit (c) and the TENG unit (d) after 4.0 m/s wind is removed. (e) Energy conversion efficiency of the ATM-TEHG under various wind speeds.

speed goes up from 2.4 to 5.0 m/s, the voltage and power outputs of the EMG unit ascend from 0.2 V/0.08 mW to 1.86 V/6.96 mW, as shown in Fig. 4f, exhibiting the superior performance of our device in exploiting the breeze energy.

## 2.5. Performance of the AMT-TEHG

In addition to the output characteristics of the TENG unit and EMG unit, the power density and energy conversion efficiency have also been computed to show the performance of the proposed AMT-TEHG, as plotted in Fig. 5. The weight power density of the TENG unit and EMG unit are evaluated by.

$$\bar{P} = \begin{cases} \frac{P_T}{M_T} & \text{TENG unit} \\ \frac{P_E}{M_E} & \text{EMG unit} \end{cases} \quad (3)$$

where  $M_T = 0.5$  g is the mass of the TENG unit, and  $M_E = 20$  g is the mass of the EMG unit. As driven by 5.0 m/s wind, the maximum weight power density of the TENG unit reaches 449.5 mW/kg, which is evidently higher than that (347.8 mW/kg) of the EMG unit although the absolute output power of the EMG unit is high, as shown in Fig. 5a. This is caused by the bulky materials (magnets and coils) required for building the EMG, which have large volume and mass and thus lead to low power density. With an increase in the wind speed from 2.4 to 5.0 m/s, the optimal weight power density of both the TENG unit and EMG unit grows almost linearly due to the increasing wind energy fed into the device, as depicted in Fig. 5b. It is apparent that the TENG unit has a higher weight power density than the EMG unit when the wind speed varies in the range from 2.4 to 5.0 m/s. The average output power of the TENG unit and EMG unit was also measured under various wind speeds, and the weight power density of the TENG unit determined with the average output power is also higher than that of the EMG unit in the wind speed range from 2.4 to 5.0 m/s, as shown in Fig. S13. In addition, both the TENG unit and the EMG unit of the AMT-TEHG exhibit high power density as compared with the typical wind-driven TENGs/TEHGs, even if the AMT-TEHG is driven by a comparatively low wind speed (5.0 m/s), as shown in Table S2. Therefore, the AMT-TEHG is well suited for exploiting the pervasive breeze energy.

The influence of the rotor weight on the TEHG working modes and output power is illustrated in Fig. S14-S16. It can be observed from the voltage output of the TENG unit that the AMT can be realized when the rotor mass is increased from the present 32 g to 38 g, as shown in Fig. S14a. However, if the rotor mass is increased to 44 g, no significant difference in the voltage amplitude of the TENG unit can be observed when the wind speed grows from 3.0 to 5.0 m/s, indicating that there is no obvious working mode transition in the TEHG. With a further increase in the rotor mass, the AMT cannot be achieved due to the limited maglev force and thus an increased wind speed is required to overcome the friction between the rotor and stator so as to start the TEHG. The increased friction with the rotor weight contributes to the enhanced output voltage of the TENG unit and in the meanwhile the reduced rotation speed. Consequently, the increased rotor weight gives rise to higher start-up wind speeds of the TEHG and lower output power from the TENG unit and the EMG unit.

The energy conversion efficiency  $\eta$  of the AMT-TEHG is defined as the ratio of the generated electric energy to the captured wind energy. For a given wind speed, the captured wind energy  $E_m$  is calculated as the maximum rotation energy of the rotor, i.e.,

$$E_m = \frac{1}{2} J \omega_m^2 \quad (4)$$

where  $J$  is the rotational inertia of the rotor and  $\omega_m$  is the maximum rotation speed of the rotor for a given wind speed. The rotation speed  $\omega_m$  can be evaluated from the voltage signal of the TENG unit or the EMG unit [46].

The generated electric energy  $E_o$  is the total output energy of the AMT-TEHG after the wind vanishes (Fig. 5c,d), which is calculated as.

$$E_o = \int I_{T,R}^2(t) R_{opt} dt + \int I_{E,R}^2(t) R_{opt} dt \quad (5)$$

where  $R_{opt}$  is the optimal resistance, which is 200 M $\Omega$  for the TENG unit and 500  $\Omega$  for the EMG unit.

Taking the output performance of the AMT-TEHG under a wind speed of 4.0 m/s for example, the captured wind energy  $E_m$  is equal to the rotation energy of the rotor in the steady state. After the wind is removed, the rotor rotates inertially and damps, enabling the EMG unit and TENG unit to generate decaying output current, as shown in Fig. 5c, d. The electric energy  $E_o$  is thus the total energy generated by the AMT-TEHG after the wind vanishes, which is converted by the device from the captured wind energy  $E_m$ . Therefore, the energy conversion efficiency  $\eta$  of the AMT-TEHG is evaluated as.

$$\eta = \frac{E_o}{E_m} \quad (6)$$

Under various wind speeds, the captured wind energy  $E_m$  and the generated electric energy  $E_o$  by the AMT-TEHG can be calculated by Eqs. (4) and (5), as shown in Fig. S17. The energy conversion efficiency of the device is then determined according to Eq. (6), as depicted in Fig. 5e. The results indicate that there is no significant difference in the energy conversion efficiency when the wind speed varies from 3.0 m/s to 5.0 m/s. With an almost constant energy conversion efficiency of around 12.3 % even at a low wind speed of 3.0 m/s, the proposed AMT-TEHG is well suited for the exploitation of the abundant breeze energy.

## 2.6. Applications of the AMT-TEHG

First, considering the intermittent availability of the natural wind energy, the alternating-current (AC) outputs from the TENG unit and the EMG unit were severally converted to direct-current (DC) electric energy using a rectifier bridge and then were accumulated in capacitors for practical utilization. For the AMT-TEHG, the rectified outputs from the two units were connected in parallel for their accumulation in the capacitor, as shown in Fig. 6a, where the device was driven by the wind of 4.5 m/s. Compared with the TENG unit, the EMG unit exhibits a fast charging rate but a low saturated voltage (2.7 V) due to its intrinsic output characteristics (large current and low voltage). By hybridizing the electric outputs from the TENG unit and the EMG unit, both fast charging rate and high voltage level can be achieved by the AMT-TEHG. Under 4.5 m/s wind, the voltage trends of various capacitors as charged by the AMT-TEHG are plotted in Fig. 6b. It can be observed that a 10  $\mu$ F capacitor could be charged to 2 V within 0.2 s, and the voltage of a comparatively large capacitor of 100  $\mu$ F could be lifted to 3.2 V from scratch within one minute, exhibiting the superior charging capability of the AMT-TEHG.

The voltage signal frequency of the TENG unit versus wind speed is depicted in Fig. 6c, which reveals a linear relationship between them. As the wind speed rises from 2.5 to 5.0 m/s, the voltage signal frequency grows almost linearly from 10.5 to 27.8 Hz. Similarly, the rotation speed of the rotor, which can be determined from the voltage signal [46], is also linearly dependent on the wind speed. The rotor speed grows linearly from 209 to 555 rpm as the wind speed ascends from 2.5 to 5.0 m/s. This excellent linear relationship provides an easy way to develop a self-sufficient wind speed sensor by extracting associated information from the voltage signal of the TENG unit, as shown in Fig. 6d. After the AMT-TEHG is driven to work by wind, the voltage signal generated by the TENG unit is input into a computer program, which was developed on the basis of LabView to calculate the wind speed based on the linear relationship between the signal frequency and the wind speed, as shown in Fig. 6c. As displayed in Fig. 6d and Movie S2, the good match between the self-sufficient wind speed sensor and a commercial anemometer demonstrates the promising application of the AMT-TEHG in self-

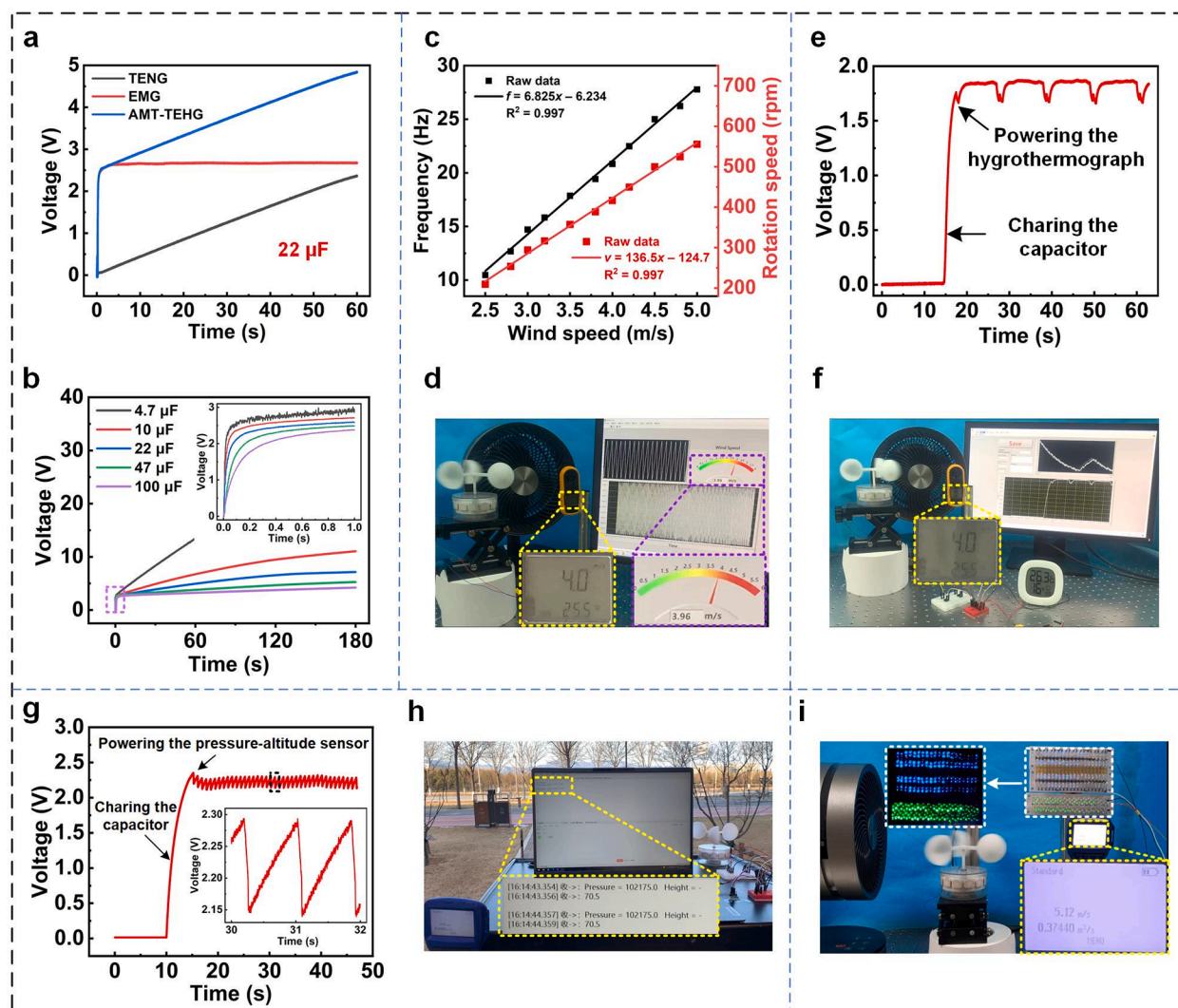


**Fig. 6.** Demonstration of the AMT-TEHG for harvesting breeze energy and sensing wind speed. (a) Voltage curves of a  $22 \mu\text{F}$  capacitor as charged by the TENG unit, EMG unit, and AMT-TEHG. (b) Voltage curves of different capacitors when charged by the AMT-TEHG. (c) The TENG output frequency and rotor speed as a function of wind speed ( $f$ ,  $v$  and  $\times$  denote the output frequency, rotor speed and wind speed, respectively). (d) A picture of self-sufficient wind speed sensor. (e) Voltage variation of a  $100 \mu\text{F}$  capacitor during powering a hygrothermograph as charged by the AMT-TEHG. (f) A picture of powering a hygrothermograph by the AMT-TEHG. (g) Voltage variation of a  $2200 \mu\text{F}$  capacitor during powering a pressure-altitude sensor by the AMT-TEHG. (h) A picture of driving a pressure-altitude sensor by the AMT-TEHG in the natural wind. (i) A picture of powering LEDs by the AMT-TEHG.

sufficient wind speed sensing.

In addition to the self-sufficient wind speed sensor, the AMT-TEHG can also act as a renewable energy source for other electronics (e.g., a hygrothermograph, a pressure-altitude sensor, and LEDs) by converting the breeze energy into electricity, as shown in Fig. 6e-i. To power a hygrothermograph, the rectified electric energy of the AMT-TEHG is first stored in a  $100 \mu\text{F}$  capacitor that acts as both a reservoir and a regulator to provide comparatively stable electric output to the sensor. Under a wind speed of around  $4.0 \text{ m/s}$ , it takes about  $1.5 \text{ s}$  for the AMT-TEHG to lift the voltage across the capacitor to the required level ( $\sim 1.8 \text{ V}$ ). After the capacitor is connected to the hygrothermograph, its voltage fluctuates slightly around  $1.8 \text{ V}$  due to the continuous and stable operation of the sensor, indicating that the AMT-TEHG can generate sufficient electric energy for the normal operation of the hygrothermograph, as demonstrated in Fig. 6e,f and Movie S3.

When positioned outdoors, the AMT-TEHG can increase the voltage of a  $2200 \mu\text{F}$  capacitor to  $2.4 \text{ V}$  within  $4 \text{ s}$  by harvesting the natural wind, as shown in Fig. 6g. After the capacitor is connected to a pressure-altitude sensor, the generated electric energy can drive the sensor to send pressure and altitude signals to a receiver at a frequency of  $1 \text{ Hz}$ , as

displayed in Fig. 6h and Movie S4. Moreover, with the rectified DC electric energy converted from the breeze of roughly  $5.0 \text{ m/s}$ , the TENG unit can light up 120 green LEDs connected in series and the EMG unit can turn on 160 blue LEDs connected in parallel, as exhibited in Fig. 6i and Movie S5.

### 3. Conclusions

In summary, we proposed a maglev mechanism-enabled AMT strategy for rotary TENGs to achieve effective harvesting of breeze energy and self-sufficient sensing of wind speed with long working duration. Enabled by a rationally designed maglev mechanism, the device can start to work in IC-mode from the idle state under a very low wind speed ( $2.4 \text{ m/s}$ ), and automatically transition to NC-mode without any tribo-materials-induced friction resistance and material abrasion with the ever increasing wind speed. With the maglev-based AMT strategy, the dissipated charges in the TENG can be replenished with significantly reduced friction drag and material wear, which contributes to superior output stability. Over a 10-day test duration, the maglev-based TENG can maintain 82 % of its incipient voltage; by contrast, the normalized

voltage of NC-TENG and C-TENG reduced to 36 % and 10 %, respectively. Moreover, the largely reduced friction drag contributes to a low start-up wind speed, which is conducive to the exploitation of the pervasive breeze energy. By introducing additional pick-up coils to the maglev-based TENG, a hybrid generator, i.e., AMT-TEHG is constructed straightforward, which enables the device to generate complementary electric outputs. By harvesting the breeze energy, the AMT-TEHG can serve as not only a self-sufficient wind speed sensor but also a renewable power source for a series of electronics, including capacitors, hygrometers, pressure-altitude sensors, and LEDs. This work demonstrates a promising strategy for realizing durable and stable TEHGs, which has promising applications in breeze energy exploitation and self-sufficient sensing.

## 4. Experimental section

### 4.1. Fabrication of the rotor

The fabricated rotor was comprised of twelve cuboidal permanent magnets (Nd-Fe-B N35), three fan-shaped FEP films, and a disk-shaped rotator with a diameter of 72 mm and thickness of 8 mm. The twelve magnets, each with a size of  $10 \times 6 \times 2 \text{ mm}^3$ , were uniformly embedded in the rotator, forming a ring-shaped array. The fan-shaped FEP films had a central angle of  $60^\circ$ , inner diameter of 20 mm, outer diameter of 66 mm, and thickness of  $25 \mu\text{m}$  for each. The three FEP films were first charged to  $-120 \text{ V}$  with a corona discharging system and then were affixed to the rotator to serve as the dielectric layer. The rotor with a centered hollow shaft was prepared from the non-transparent photopolymer by the 3D printing technology.

### 4.2. Fabrication of the stator

The fabricated stator consisted of a printed circuit board (PCB), multiple cuboidal permanent magnets, twelve sets of pick-up coils, and a disk-shaped substrate. The PCB is 66 mm in diameter, on which two copper electrodes were deposited in a complementary pattern. Each of the electrode comprises three sectors of copper film, and the central angle of each copper film is approximately  $59^\circ$ . The permanent magnets embedded in the substrate of the stator are identical to those positioned in the rotor. The twelve pick-up coils, with 300 turns for each, were made of varnished wire and arranged in a ring encircling the stator. The disk-shaped substrate, which was 3D-printed from the non-transparent photopolymer, has a diameter of 74 mm, thickness of 6 mm, and a central hole of 3.9 mm in diameter for fixing the stainless steel shaft.

### 4.3. Assemblage of AMT-TEHG

To realize the automatic transition between the IC-mode and NC-mode, a bearing was used to assemble the rotor and stator. The bearing has an internal diameter of 4 mm, allowing 0.1 mm interspace between the bearing (inner race) and the stainless steel shaft. The assembled rotor and stator were encapsulated in a cylindrical housing. The wind cups and the rotating shaft, which were fabricated from the non-transparent photopolymer by 3D-printing technology, were connected to the rotor by inserting the rotating shaft into the hollow shaft of the rotor. The wind cup has a diameter of 50 mm and arm length of 23 mm. The lid of the housing was designed with a central hole, through which the rotating shaft and the lid were assembled via a bearing with an internal diameter of 5 mm and outer diameter of 11 mm. The main body of the device, excluding the wind cups, is 40 mm high and 82 mm in diameter.

### 4.4. Electrical measurement

In the motor-driven test, a stepper motor (DE60HB102-1000, DVS Mechatronics, China) was employed to spin the AMT-TEHG. In the wind

energy harvesting test, an air blower (FSTZ-20X60Bg3, Gree, China) was used to provide the breeze. In different tests, an electrometer (6514, Keithley, USA) was employed to measure the electric outputs of the AMT-TEHG.

## CRedit authorship contribution statement

**Kangqi Fan:** Conceptualization, Writing – original draft, Funding acquisition. **Chenggen Chen:** Investigation, Data curation, Investigation. **Baosen Zhang:** Investigation, Validation, Software. **Xiang Li:** Methodology, Resources. **Zhen Wang:** Investigation, Formal analysis. **Tinghai Cheng:** Conceptualization, Resources, Writing – review & editing, Supervision. **Zhong Lin Wang:** Conceptualization, Project administration, Writing – review & editing, Supervision.

## Declaration of Competing Interest

The authors declare that they have no known competing financial interests or personal relationships that could have appeared to influence the work reported in this paper.

## Data availability

Data will be made available on request.

## Acknowledgements

This research is supported by the National Natural Science Foundation of China (No. 52077159) and Beijing Natural Science Foundation (No. 3222023).

## Appendix A. Supplementary material

Supplementary data to this article can be found online at <https://doi.org/10.1016/j.apenergy.2022.120218>.

## References

- [1] Wang ZL. Entropy theory of distributed energy for internet of things. *Nano Energy* 2019;58:669–72.
- [2] Liu L, Guo X, Liu W, Lee C. Recent progress in the energy harvesting technology—from self-powered sensors to self-sustained iot, and new applications. *Nanomaterials* 2021;11:2975.
- [3] Guo X, He T, Zhang Z, Luo A, Wang F, Ng EJ, et al. Artificial intelligence-enabled caregiving walking stick powered by ultra-low-frequency human motion. *ACS Nano* 2021;15:19054–69.
- [4] Wang J, Ding W, Pan L, Wu C, Yu H, Yang L, et al. Self-powered wind sensor system for detecting wind speed and direction based on a triboelectric nanogenerator. *ACS Nano* 2018;12:3954–63.
- [5] Guo X, Liu L, Zhang Z, Gao S, He T, Shi Q, et al. Technology evolution from micro-scale energy harvesters to nanogenerators. *J Micromech Microeng* 2021;31:093002.
- [6] Fu X, Xu S, Gao Y, Zhang X, Liu G, Zhou H, et al. Breeze-wind-energy-powered autonomous wireless anemometer based on rolling contact-electrification. *ACS Energy Lett* 2021;6:2343–50.
- [7] Archer CL, Jacobson MZ. Evaluation of global wind power. *J Geophys Res Atmos* 2005;110:D12110.
- [8] Liu L, Guo X, Lee C. Promoting smart cities into the 5g era with multi-field internet of things (iot) applications powered with advanced mechanical energy harvesters. *Nano Energy* 2021;88:106304.
- [9] Fan F-R, Tian Z-Q, Lin WZ. Flexible triboelectric generator. *Nano Energy* 2012;1:328–34.
- [10] Wang ZL, Wang AC. On the origin of contact-electrification. *Mater Today* 2019;30:34–51.
- [11] Wang ZL. From contact electrification to triboelectric nanogenerators. *Rep Prog Phys* 2021;84:096502.
- [12] Feng Y, Jiang T, Liang X, An J, Wang ZL. Cylindrical triboelectric nanogenerator based on swing structure for efficient harvesting of ultra-low-frequency water wave energy. *Appl Phys Rev* 2020;7:021401.
- [13] Chen J, Huang Y, Zhang N, Zou H, Liu R, Tao C, et al. Micro-cable structured textile for simultaneously harvesting solar and mechanical energy. *Nat Energy* 2016;1:16138.

- [14] Long L, Liu W, Wang Z, He W, Li G, Tang Q, et al. High performance floating self-excited sliding triboelectric nanogenerator for micro mechanical energy harvesting. *Nat Commun* 2021;12:4689.
- [15] Xu W, Zheng H, Liu Y, Zhou X, Zhang C, Song Y, et al. A droplet-based electricity generator with high instantaneous power density. *Nature* 2020;578:392–6.
- [16] Lin S, Xu L, Chi Wang A, Wang ZL. Quantifying electron-transfer in liquid-solid contact electrification and the formation of electric double-layer. *Nat Commun* 2020;11:399.
- [17] Wang J, Wu Z, Pan L, Gao R, Zhang B, Yang L, et al. Direct-current rotary-tubular triboelectric nanogenerators based on liquid-dielectrics contact for sustainable energy harvesting and chemical composition analysis. *ACS Nano* 2019;13:2587–98.
- [18] Zhou Z, Weng L, Tat T, Libanori A, Lin Z, Ge L, et al. Smart insole for robust wearable biomechanical energy harvesting in harsh environments. *ACS Nano* 2020;14:14126–33.
- [19] Zhang B, Zhang S, Li W, Gao Q, Zhao D, Wang ZL, et al. Self-powered sensing for smart agriculture by electromagnetic-triboelectric hybrid generator. *ACS Nano* 2021;15:20278–86.
- [20] He Q, Wu Y, Feng Z, Sun C, Fan W, Zhou Z, et al. Triboelectric vibration sensor for a human-machine interface built on ubiquitous surfaces. *Nano Energy* 2019;59:689–96.
- [21] Pu X, Guo H, Chen J, Wang X, Xi Y, Hu C, et al. Eye motion triggered self-powered mechnosensational communication system using triboelectric nanogenerator. *Sci Adv* 2017;3:e1700694.
- [22] Li X, Cao Y, Yu X, Xu Y, Yang Y, Liu S, et al. Breeze-driven triboelectric nanogenerator for wind energy harvesting and application in smart agriculture. *Appl Energy* 2022;306:117977.
- [23] Zhang C, Liu Y, Zhang B, Yang O, Yuan W, He L, et al. Harvesting wind energy by a triboelectric nanogenerator for an intelligent high-speed train system. *ACS Energy Lett* 2021;6:1490–9.
- [24] Ye C, Dong K, An J, Yi J, Peng X, Ning C, et al. A triboelectric–electromagnetic hybrid nanogenerator with broadband working range for wind energy harvesting and a self-powered wind speed sensor. *ACS Energy Lett* 2021;6:1443–52.
- [25] Luo J, Wang ZL. Recent progress of triboelectric nanogenerators: From fundamental theory to practical applications. *EcoMat* 2020;2:e12059.
- [26] Zou H, Guo L, Xue H, Zhang Y, Shen X, Liu X, et al. Quantifying and understanding the triboelectric series of inorganic non-metallic materials. *Nat Commun* 2020;11:2093.
- [27] Chen P, An J, Shu S, Cheng R, Nie J, Jiang T, et al. Super-durable, low-wear, and high-performance fur-brush triboelectric nanogenerator for wind and water energy harvesting for smart agriculture. *Adv Energy Mater* 2021;11:2003066.
- [28] Yong S, Wang J, Yang L, Wang H, Luo H, Liao R, et al. Auto-switching self-powered system for efficient broad-band wind energy harvesting based on dual-rotation shaft triboelectric nanogenerator. *Adv Energy Mater* 2021;11:2101194.
- [29] Wang Y, Yu X, Yin M, Wang J, Gao Q, Yu Y, et al. Gravity triboelectric nanogenerator for the steady harvesting of natural wind energy. *Nano Energy* 2021;82:105740.
- [30] Wang S, Xie Y, Niu S, And LL, Wang ZL. Freestanding triboelectric-layer-based nanogenerators for harvesting energy from a moving object or human motion in contact and non-contact modes. *Adv Mater*. 2014;26:2818–24.
- [31] Lin Z, Zhang B, Xie Y, Wu Z, Yang J, Wang ZL. Elastic-connection and soft-contact triboelectric nanogenerator with superior durability and efficiency. *Adv Funct Mater* 2021;31:2105237.
- [32] Lin L, Xie Y, Niu S, Wang S, Yang P-K, Wang ZL. Robust triboelectric nanogenerator based on rolling electrification and electrostatic induction at an instantaneous energy conversion efficiency of ~55%. *ACS Nano* 2015;9:922–30.
- [33] Guo H, Chen J, Yeh M-H, Fan X, Wen Z, Li Z, et al. An ultrarobust high-performance triboelectric nanogenerator based on charge replenishment. *ACS Nano* 2015;9:5577–84.
- [34] Li X, Luo J, Han K, Shi X, Ren Z, Xi Y, et al. Stimulation of ambient energy generated electric field on crop plant growth. *Nat Food* 2022.
- [35] Chen J, Wei X, Wang B, Li R, Sun Y, Peng Y, et al. Design optimization of soft-contact freestanding rotary triboelectric nanogenerator for high-output performance. *Adv Energy Mater* 2021;11:2102106.
- [36] Han J, Feng Y, Chen P, Liang X, Pang H, Jiang T, et al. Wind-driven soft-contact rotary triboelectric nanogenerator based on rabbit fur with high performance and durability for smart farming. *Adv Funct Mater* 2022;32:2108580.
- [37] Zhong Y, Guo Y, Wei X, Rui P, Du H, Wang P. Multi-cylinder-based hybridized electromagnetic-triboelectric nanogenerator harvesting multiple fluid energy for self-powered pipeline leakage monitoring and anticorrosion protection. *Nano Energy* 2021;89:106467.
- [38] Chen J, Guo H, Hu C, Wang ZL. Robust triboelectric nanogenerator achieved by centrifugal force induced automatic working mode transition. *Adv Energy Mater* 2020;10:2000886.
- [39] Lin Z, Zhang B, Zou H, Wu Z, Guo H, Zhang Y, et al. Rationally designed rotation triboelectric nanogenerators with much extended lifetime and durability. *Nano Energy* 2020;68:104378.
- [40] Fan K, Wei D, Zhang Y, Wang P, Tao K, Yang R. A whirligig-inspired intermittent-contact triboelectric nanogenerator for efficient low-frequency vibration energy harvesting. *Nano Energy* 2021;90:106576.
- [41] Akoun G, Yonnet JP. 3d analytical calculation of the forces exerted between two cuboidal magnets. *IEEE T Magn* 1984;20:1962–4.
- [42] Wu H, Wang S, Wang Z, Zi Y. Achieving ultrahigh instantaneous power density of 10 mw/m<sup>2</sup> by leveraging the opposite-charge-enhanced transistor-like triboelectric nanogenerator (oct-teng). *Nat Commun* 2021;12:5470.
- [43] Jiang T, Pang H, An J, Lu P, Feng Y, Liang X, et al. Robust swing-structured triboelectric nanogenerator for efficient blue energy harvesting. *Adv Energy Mater* 2020;10:2000064.
- [44] Zhu G, Chen J, Zhang T, Jing Q, Wang ZL. Radial-arrayed rotary electrification for high performance triboelectric generator. *Nat Commun* 2014;5:3426.
- [45] Liu H, Hou C, Lin J, Li Y, Shi Q, Chen T, et al. A non-resonant rotational electromagnetic energy harvester for low-frequency and irregular human motion. *Appl Phys Lett* 2018;113:203901.
- [46] Fan K, Liang G, Wei D, Wang W, Zhou S, Tang L. Achieving high-speed rotations with a semi-flexible rotor driven by ultralow-frequency vibrations. *Appl Phys Lett* 2020;117:223901.